Task-Based Design of Fluence Field Modulation in CT for Model-Based Iterative Reconstruction

Grace J. Gang, Jeffrey H. Siewerdsen, and J. Webster Stayman

***Abstract* — A task-driven imaging framework for prospective fluence field modulation (FFM) is developed in this paper. The design approach uses a system model that includes a parameterized FFM acquisition and model-based iterative reconstruction (MBIR) for image formation. Using prior anatomical knowledge (e.g. from a low-dose 3D scout image), accurate predictions of spatial resolution and noise as a function of FFM are integrated into a task-based objective function. Specifically, detectability index (*d'*), a common metric for task-based image quality assessment, is computed for a specific formulation of the imaging task. To optimize imaging performance in across an image volume, a maximin objective function was adopted to maximize the minimum detectability index for many locations sampled throughout the volume. To reduce the dimensionality, FFM patterns were represented using wavelet bases, the coefficients of which were optimized using the covariance matrix adaptation evolutionary strategy (CMA-ES) algorithm. The optimization was performed for a mid-frequency discrimination task involving a cluster of micro-calcifications in an abdomen phantom. The task-driven design yielded FFM patterns that were significantly different from traditional strategies proposed for FBP reconstruction. In addition to a higher minimum *d'* consistent with the objective function, the task-driven approach also improved *d'* to a greater extent over a larger area of the phantom. Results from this work suggests that FFM strategies suitable for FBP reconstruction need to be reevaluated in the context of MBIR and that a task-driven imaging framework provides a promising approach for such optimization.**

***Index Terms*—Task-based optimization, detectability index, model-based reconstruction, fluence field modulation, CT**

I. Introduction

Computed tomography plays an invaluable role in diagnostic imaging, yet increased usage and public concern about risk associated with ionizing radiation has motivated a large body of research in dose reduction techniques. [1] Among such efforts, there has been increased interest in integrating fluence field modulation (FFM) devices with diagnostic CT. [2]–[4] Compared to automatic exposure control on current scanners, FFM permits much greater freedom in shaping the dose distribution in the patient as well as satisfying more flexible (e.g., spatially-varying or uniform) image quality requirements in the reconstructed image. While previous work has concentrated largely on FFM designs for filtered-backprojection (FBP) reconstruction, this work extends such investigation to model-based iterative reconstruction (MBIR).

It is widely acknowledged that dose reduction techniques must be coupled with image quality needs [5] and that image performance metrics need to be defined based on the imaging task [6]. Towards this end, in this work, we present a task-driven imaging approach to prospectively optimize FFM based on prior specification of the imaging task (e.g., based on disease prevalence, anatomical target, etc.) and the patient anatomy (e.g., from a very low dose 3D scout acquisition). This framework is developed for MBIR using predictors of noise and resolution properties that may be integrated into an expression for task-based detectability. We compare conventional FFM strategies (typically designed based on FBP reconstruction) and the task-driven FFM approach using a penalized-likelihood reconstruction.

II. Theoretical Methods

A. Task-Driven Imaging Framework

Task-driven frameworks have previously been used in the context of regularization optimization [7], tube current modulation [8], source-detector trajectory [9]. Figure 1 presents a general task-driven imaging framework. Central to the framework is an optimization loop to identify acquisition parameters (Ω_A) and reconstruction parameters (Ω_R) of interest that maximizes an objective function based on a task-based image quality metric - detectability index (*d'*).

The mathematical form of *d'* is given in Eq.1, corresponding to a non-pre-whitening observer model:

$$d'^2(\Omega_A,\Omega_R)=\frac{\left[\iiint |T(\Omega_A,\Omega_R)\cdot W_{Task}|^2 df_x df_y df_z\right]^2}{\iiint S(\Omega_A,\Omega_R)|T(\Omega_A,\Omega_R)\cdot W_{Task}|^2 df_x df_y df_z} \qquad (1)$$

where T and S respectively represents the local modulation transfer function (MTF) and noise power spectrum (NPS) in the reconstructed image and can be predicted by the system model. The MTF and NPS carry dependence on both (Ω_A,Ω_R) and the patient-specific measurements computed from the anatomical model provided by a low-dose 3D scout. In diagnostic imaging, the imaging task can be predefined based on suspected abnormalities and disease prevalence in the anatomical site to be imaged.

In these initial investigations, binary classification tasks were considered, where the task function, W_{Task}, corresponds to the difference between the Fourier transform of two possible outcomes (e.g., one signal vs. another, or signal-present vs. signal absent which simplifies to a detection task).

This work is supported by NIH grant U01EB018758. G. J. Gang, J. W. Stayman, and J. H. Siewerdsen are with the Department of Biomedical Engineering, Johns Hopkins University, Baltimore, MD 21205 USA (e-mail: {grace.j.gang, web.stayman, jeff.siewerdsen}@jhu.edu).

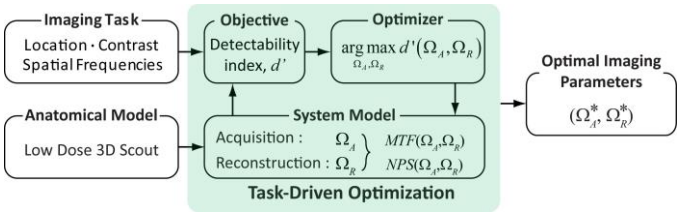

Fig.1. Framework for task-driven imaging.

B. Quadratic Penalized Likelihood Reconstruction

The MBIR method investigated in this work adopts a penalized-likelihood (PL) objective whose solution is given by:

$$\hat{\mu} = \underset{\mu}{\operatorname{argmax}}[\log L(\mu; y) - \beta R(\mu)], \qquad (2)$$

where $L(\mu; y)$ is the likelihood term, $R(\mu)$ is a roughness penalty, and β controls the tradeoff between the two. The measurements, y, are assumed to be independent and Poisson-distributed, with means given by the following forward model:

$$\bar{y} = I_0 e^{-\mathbf{A}\mu} \qquad (3)$$

where I_0 is the number of bare-beam photons per detector pixel and $\mathbf{A}$ is the forward projection operator. We adopt a traditional quadratic roughness penalty with first-order neighborhood.

C. System Model for Fast Prediction for Noise and Resolution

The noise and resolution predictors for PL reconstruction are based on previous derivations in Refs [10], [11], [12]. Both the spatial resolution and noise are spatially varying in a PL reconstruction. Thus, the MTF, NPS, and *d'* are only meaningful in a local context. [7] A Fourier approximation of the MTF and NPS is given by:

$$T_j \approx \frac{\mathcal{F}\{\mathbf{A}^T D\{\bar{y}(\mu)\}\mathbf{A}e_j\}}{\mathcal{F}\{\mathbf{A}^T D\{\bar{y}(\mu)\}\mathbf{A}e_j + \beta\mathbf{R}e_j\}} \qquad 4(a)$$

$$S_j \approx \frac{\mathcal{F}\{\mathbf{A}^T D\{\bar{y}(\mu)\}\mathbf{A}e_j\}}{\left|\mathcal{F}\{\mathbf{A}^T D\{\bar{y}(\mu)\}\mathbf{A}e_j + \beta\mathbf{R}e_j\}\right|^2} \qquad 4(b)$$

where subscript j denotes voxel location and e_j is the j-th unit vector. The operator $D\{\cdot\}$ converts its vector argument to a diagonal matrix and $\mathbf{R}$ is the Hessian matrix of the quadratic penalty that is independent of μ or $\bar{y}$.

Since a large number of evaluations of Eq.4 and Eq.1 are required for optimization, several techniques were adopted to speed up computation. First, using $\mathbf{i}$ to denote projection number, $\mathcal{F}\{\mathbf{A_i}^T\mathbf{A_i}e_j\}$ is precomputed and stored for each projection. This expression is scaled by the appropriate $\bar{y}_j$ according to a specific FFM (which determines y) and is summed over all projections to get $\mathcal{F}\{\mathbf{A}^T D\{\bar{y}(\mu)\}\mathbf{A}e_j\}$. Second, $\mathcal{F}\{\mathbf{A_i}^T\mathbf{A_i}e_j\}$ was assumed to be independent of voxel location j, i.e., only one set of $\mathcal{F}\{\mathbf{A_i}^T\mathbf{A_i}e_j\}$ needs to be stored for *d'* calculation in multiple locations. Such an assumption is reasonable for good angular sampling and voxel locations in the central plane. Lastly, instead of using the full image volume support for e_j, $\mathcal{F}\{\mathbf{A_i}^T\mathbf{A_i}e_j\}$ is only computed and stored for a 49×49×49 voxel VOI centered at j. The VOI size is chosen to be bigger than the correlation length between voxels. Since $\mathbf{R}$ is independent of μ or $\bar{y}$, $\mathcal{F}\{\beta\mathbf{R}e_j\}$ only needs to be precomputed once and stored. These techniques allows fast computation of the MTF, NPS and *d'* – e.g., evaluating *d'* for 50 voxel locations requires 0.06 s.

D. Low Dimensional Parameterization of Fluence Field

An arbitrary fluence field could potentially be specified for each horizontal detector element (denoted as u) and each projection number (denoted as p). Thus, a modulated fluence field pattern is a 2D function on (u, p). To reduce the dimensionality of the optimization, and to enforce smoothness constraints, we parameterize the fluence field (FF) using coefficents for a set of 2D wavelet bases, such that

$$FF(u,p) = \sum_i^n \omega_{\text{ff}}^i \mathrm{B}^i(u,p) \qquad (5)$$

This permits low-dimensional estimation of the coefficient vector, $\vec{\Omega}_{\text{ff}} = [\omega_{\text{ff}}^1, \omega_{\text{ff}}^2, \ldots, \omega_{\text{ff}}^n]^T$. Practical FFM systems are likely to be smoothly-varying in both u and p. That is, x-ray beam profiles are spatially smooth and do not change abruptly from angle to angle. For this reason, the basis functions, $\mathrm{B}^i(\vec{r})$, were chosen to be 2D Gaussian wavelets on (u, p). In addition, projections traversing the same voxel that are 180° apart are assumed to have the same fluence to enforce a symmetric design in 360° rotations. An example set of wavelet functions are illustrated in Fig.2 with coarse sampling along both directions. For the actual optimization, the Gaussians are centered at 17 locations in u and 6 locations in p, giving a total of 17×6=102 coefficients.

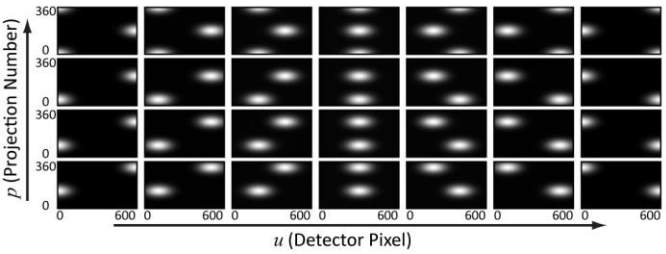

Fig.2. Wavelet bases for low dimensional parameterization of fluence field.

E. Objective Function and Optimizer

To optimize FFM, *d'* values over multiple locations within the reconstruction need to be considered. There are many ways to formulate an objective function, e.g., maximize the mean *d'*, equalizing *d'*, etc. In this work, a maximin objective is used to maximize the minimum *d'*, i.e.:

$$\max_{\vec{\Omega}_{\text{ff}}} \min_{\vec{v}} d'(\vec{v}; \vec{\Omega}_{\text{ff}}) \quad \text{s.t.} \quad \sum_{(u^*,p)} FF(u^*, p) = I_{tot} \qquad (6)$$

where $\vec{v}$ is the coordinate vector for the 3D reconstructed image and represent a set of discrete points within the object over which *d'* is evaluated. By maximizing the minimum *d'*, one guarantees a specific level of detectability in the volume. The optimization is subjected to a total exposure constraint (the sum of the barebeam fluence over all projections and detector locations behind the object, denoted u^*). Due to the non-linear, non-convex nature of the problem, a stochastic and derivative-free optimizer - Covariance Matrix Adaptation Evolution Strategy (CMA-ES) [13] is used to solve this objective.

III. Experimental Methods

A. Phantom and Imaging Task

The CT scan of a cadaver abdomen was used as a digital phantom. The central plane is illustrated in Fig.3(a) with a large number of stimuli shown in Fig.3(b) inserted at locations randomly perturbed around a 11×16 grid. The imaging task is the "detection" of a calcification cluster constructed of three

Gaussian stimuli (width=0.8 mm) evenly distributed along the perimeter of a 4mm diameter circle. Specifically the task is to discriminate the three calcification cluster from a monolithic stimulus – a Gaussian with width equal to 4 mm. We enforce a task definition where all rotational orientations are equally likely (e.g. a symmetric task function). Specifically, the task function is equal to the Hankel transform of the Fourier transform of the stimulus minus the Fourier transform of the larger Gaussian, the result of which is plotted in Fig.3(c).

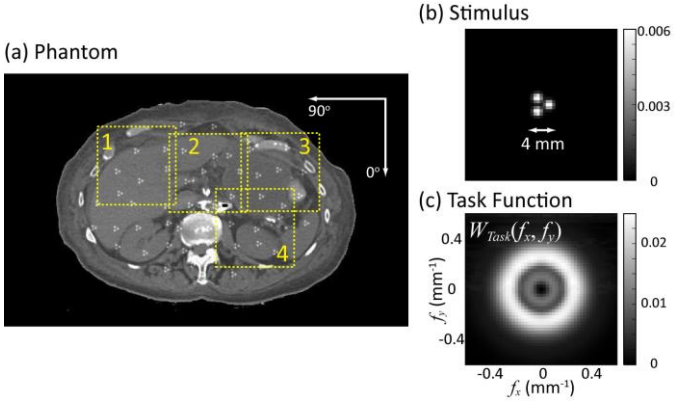

Fig.3. (a) The abdomen phantom is based on a diagnostic CT scan of a cadaver. (b) The stimulus consisting of three narrow Gaussians simulating a cluster of micro-calcifications. (c) The Fourier domain task function corresponding to the discrimination of (b) from a larger Gaussian stimulus. Rotational symmetry is introduced to account for other orientations of the cluster.

B. Image Simulation and Reconstruction

A bare beam fluence of 2.5×10^4 to 4.5×10^4 photons/mm^2 was used to simulate projection images. We considered a system geometry with an 80 cm source-to-axis distance and a 120 cm source-to-detector distance. The detector pixel size was 1.3×1.3 mm and reconstruction voxel size was 0.87×0.87×0.87 mm. A GPU-implemented linear projector was used. Penalized-likelihood reconstruction was performed using 80 iterations of paraboloidal surrogate updates with 20 ordered-subsets in the first 40 iterations and 1 subset in the last 40 to encourage convergence.

C. Comparison with Other Strategies

The task-driven fluence field design was compared with three other strategies. All strategies were subjected to the same total fluence constraint in Eq.6.

(1) Unmodulated: Constant bare-beam fluence with no modulation as a function of either u or p.

(2) Flat fluence on the detector (denoted as "Flat"): Extending the parameterization developed by Gies et al. from tube current modulation to FFM, the fluence field can be expressed as a function of the line integral, l, and a scalar, α, as:

$$FF(u^*,p) = \frac{e^{\alpha l(u^*,p)}}{\sum_p e^{\alpha l(u^*,p)}} I_0^{tot}. \quad (7)$$

When $\alpha = 1$, the fluence behind the object incident on the detector becomes flat. This modulation pattern is attractive because the reconstructed image would have isotropic and uniform noise and resolution (hence d') throughout the image.

(3) Extension of the Minimum variance solution in FBP (denoted as "$\alpha = 0.5$"): Gies et al. derived that when $\alpha = 0.5$, the tube current modulation simplified from Eq.7 by tracing the detector elements corresponding to one voxel location achieves minimum variance in that particular voxel in an FBP reconstruction. Rather than setting a single tube current value per projection angle, we extend this approach to FFM by applying the same strategy to compute a beam shape. The third FFM is calculated from Eq.7 when $\alpha = 0.5$.

D. Image Quality Assessment

Detectability index was computed for locations on a 11×16 grid within the phantom (including skin line) and interpolated using radial basis functions to obtain a detectability map, $d'(x, y)$. Reconstructions using FFM from all four strategies were presented for the four ROIs illustrated in Fig.3(a) for visual assessment.

IV. Results

The fluence field for all three strategies are shown in Fig.4. The $\alpha = 1.0$ field peaks at projections at 90° and 270° degrees which traverse the lateral direction of the phantom. The $\alpha = 0.5$ strategy follows the same trend, but the modulation is smaller. Interestingly, the task-driven fluence field is the opposite of the previous two, with peak fluence around 0°, 180°, and 360°.

This trend can be explained by the local MTF and NPS plots in Fig.5. (Only one location at the center of the image is shown for brevity.) Both the MTF and NPS are anisotropic according to the stastical weighting in each view and applying FFM can, to a certain degree, control the noise-resolution tradeoff with respect to an imaging task. Quadratic PL penalizes noisy data more heavily, resulting in MTF and NPS with almost complementary shapes, i.e., radial directions corresponding to low noise projection data has intrinsically higher resolution and vice versa. The task-driven approach takes advantage of this behavior and further enhances spatial resolution along the f_x direction by increasing fluence in anterior-posterior views, thus boosting signal power [numerator of d' in Eq.1]. Although noise is increased along the f_y direction, the intrinsic smoothing of PL alleviates this effect and d' is improved overall.

The detectability map, $d'(x, y)$, for the Unmodulated, Flat, $\alpha = 0.5$, and Task-Driven strategies are shown in Fig.6 with the minimum d' value superimposed. As expected, $d'(x, y)$ for the

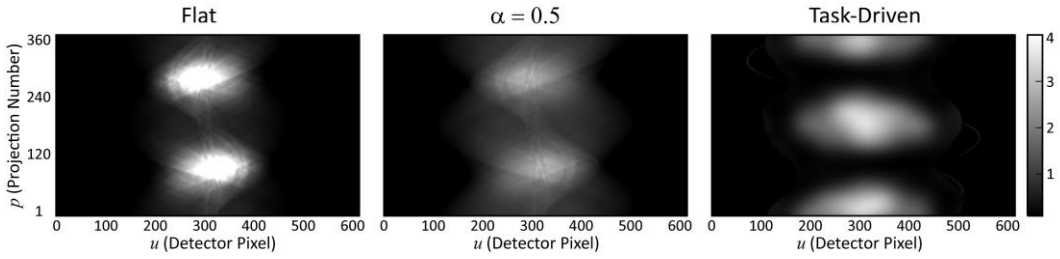

Fig.4. Fluence field modulation patterns for the Flat, $\alpha = 0.5$, and Task-Driven strategies.

Unmodulated strategy is the lowest at the center (minimum d'=0.92) and gradually increases towards the edge of the phantom. In comparison, the Flat field results in uniform d' throughout, therefore improving d' at the center but decrease d' at the edge, with a minimum (uniform) d' of 1.25. The $\alpha = 0.5$ field has a d' map that falls between the previous two cases with a minimum d' of 1.06. Relative to the unmodulated case, d' is improved for a larger area over the phantom but to a lesser degree compared to the "Flat" field. The task-driven approach achieved higher minimum d' (=1.36) than other strategies. This is consistent with the maximin objective, according to which the rank order follows Task-driven > Flat > $\alpha = 0.5$ > Unmodulated. The task-driven $d'(x, y)$ is almost uniform within the ribcage where the optimization was performed, suggesting that there is more than one solution that can achieve uniform d'. In addition to a higher minimum d', the task-driven case also achieved a higher d' at every location compared to the Flat field, and improved d' in a large area around the center of the phantom compared to the Unmodulated and $\alpha = 0.5$ strategies.

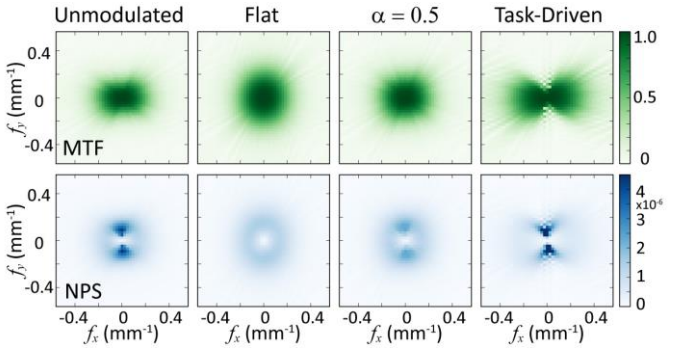

Fig.5. The local MTF (top row) and NPS (bottom row) at the center of the reconstruction for the four FFM strategies.

Trends in d' are generally supported by the reconstructions shown Fig.7 using the four FFM strategies (columns) for the four ROIs (rows) in Fig.3(a). In both the Unmodulated and $\alpha = 0.5$ reconstructions, the imaging task (i.e., distinguish the three separate dots) is visibly easier to perform at the edge of the phantom (left side of ROI 1, upper right corner of ROI 3) than the center (ROIs 2 and 4). The Flat and Task-driven FFM, on the other hand, achieve relative uniform performance across all four ROIs. Comparing across strategies, on the edge of the phantom, the imaging task is the easiest to perform in the unmodulated strategy compared to all others. An example stimulus is marked by the yellow arrow in ROI 1. As one moves towards the right of ROI 1 (i.e., towards the center of the phantom), the Unmodulated reconstruction starts to deteriorate and the task-driven strategy starts showing greater performance as seen by the stimulus indicated by the red arrow. At the center of the phantom (ROIs 2 and 4), the task-driven strategy outperforms the rest, followed closely by the Flat field. Both the unmodulated and $\alpha = 0.5$ strategies fall short in these regions. Example stimuli are indicated in ROIs 2 and 4.

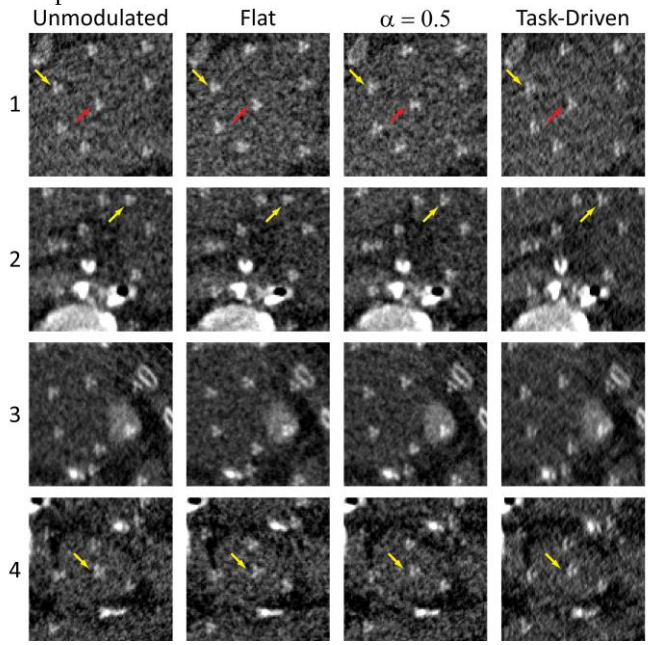

Fig.7. Reconstructions using fluence field modulation from the four imagine strategies (columns) in four ROIs (rows) in the abdomen phantom illustrated in Fig.3(a).

V. DISCUSSION AND CONCLUSIONS

This work presented FFM optimization for MBIR within a task-driven imaging framework. For the mid-frequency task in this investigation, the task-driven approach outperformed conventional strategies originally proposed for FBP reconstruction and yielded unconventional modulation patterns. This suggests that imaging strategies suitable for FBP needs to be reevaluated in the context of MBIR and the task-driven imaging framework provides a promising approach in optimizing imaging performance.

REFERENCES

[1] F. A. Mettler, et al., *Health Phys.*, vol. 95, no. 5, pp. 502–7, Nov. 2008.
[2] S. S. Hsieh and N. J. Pelc, *SPIE Medical Imaging*, 2013, p. 86681Q.
[3] T. P. Szczykutowicz et al., *Phys. Med. Biol.*, vol. 59, no. 5, pp. 1305, 2014.
[4] S. Bartolac, et al., *Med. Phys.*, vol. 38 Suppl 1, p. S2, Jul. 2011.
[5] C. H. McCollough, et al.. *AJR.*, vol. 193, no. 1, pp. 28–39, Jul. 2009.
[6] P. F. Sharp, et al. *Int. Comm. Radiol. Units Meas. (Bethesda, Md)*, 1996.
[7] G. J. Gang, et al., *Med. Phys.*, vol. 41, no. 8, p. 081902, Aug. 2014.
[8] G. J. Gang, et al., *Phys. Med. Biol.*, vol. 60, no.8, p.3129-50, 2015.
[9] Stayman et al., *Proc. Fully 3D*, 2012, pp. 257–260.
[10] J. A. Fessler, *IEEE Trans.*, vol. 5, no. 3, pp. 493–506, Jan. 1996.
[11] Y. Zhang-O'Connor et al., *IEEE Trans.*, vol. 26, no. 3, pp. 335, 2007.
[12] J. W. Stayman et al. *IEEE Trans.*, vol. 23, no. 12, pp. 1543, Dec. 2004.
[13] N. Hansen, et al. *ICGA*, 1995, pp. 57–64.

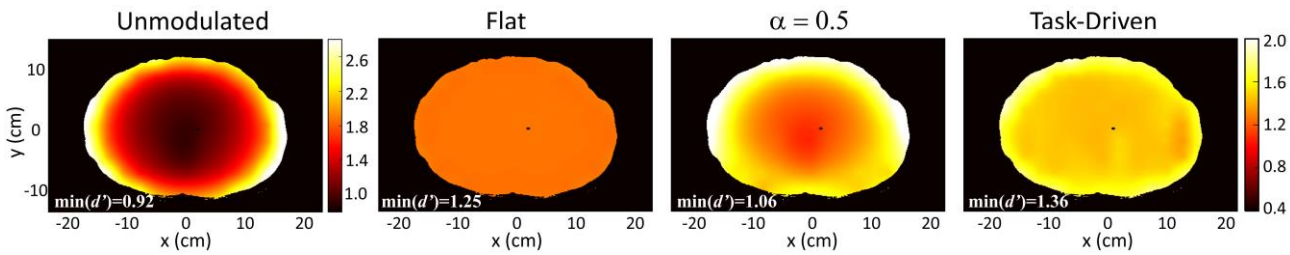

Fig.6. Detectability index maps $d'(x, y)$ for the four FFM strategies,